INTERNATIONAL JOURNAL FOR NUMERICAL AND ANALYTICAL METHODS IN GEOMECHANICS
Int. J. Numer. Anal. Meth. Geomech. 2016; **00**:1–22
Published online in Wiley InterScience (www.interscience.wiley.com). DOI: 10.1002/nag

Comprehensive study of the drying behavior of Boom clay : experimental investigation and numerical modeling

J.Hubert[1,4*], E. Plougonven[2], N. Prime[3], A. Leonard[2], F. Collin[1]

[1]*Department ArGEnCo, University of Liège, Belgium,*[2]*Dpt. Chimie appliquée, University of Liège, Belgium,*[3]*University Savoie Mont-Blanc LOCIE, France,*[4]*FRS-FNRS, Fonds National de la Recherche Scientifique*

SUMMARY

This paper presents a thermo-hydro-mechanical framework to model the drying behavior of Boom Clay. First, the experimental campaign conducted by Prime *et al* [1] is briefly presented since it is used to validate the model. The data acquisition and processing is emphasized because of the use of X-ray microtomography to be able to more accurately compare experimental and numerical strain fields.The different sub-models are introduced. Numerical simulations are performed to illustrate the capability of the proposed model to reproduce the observed behavior. Finally, a comprehensive sensitivity study on several key model parameters associated with the water retention curve, and the permeability of the medium is performed to get a better understanding of the physics behind the coupled model. Copyright © 2016 John Wiley & Sons, Ltd.

Received . . .

KEY WORDS: Porous medium ; Convective drying ; Mass and heat transfer ; Shrinkage ; X-ray microtomography

1. INTRODUCTION

Nuclear power plants produce energy efficiently but also generate long-lived highly radioactive waste. The later is hazardous to both environment and human health, and needs to be isolated from the biosphere until the radioactivity has sufficiently decayed. For that reason, it is subject to very restrictive regulations by national agencies: in Belgium, isolation procedures are based on a waste classification established by ONDRAF (Organisme National des Déchets Radioactifs et des matières Fissiles enrichies) in collaboration with the European Commission [2]. The scientific community is therefore faced with the task of finding technical solutions to respect those regulations. The long term management of high activity waste is internationally studied and the most promising solution seems to be deep geological storage [3].

1.1. Deep geological storage

Waste isolation is guaranteed by the combination of natural and engineered barriers, referred to as the multi-barriers principle. The natural barrier is the geological layer, preferably with a very low permeability [4]. In Belgium, the principle for the engineered barrier is visible on Figure 1.

These layers make up the super-containers that, following the belgian prescriptions, will be placed within tunnels over 200 m deep. These tunnels will then be backfilled with a granular material (such as a mix of sand and bentonite) to prevent collapse of the gallery, provide a good enough

*Correspondence to: julien.hubert@ulg.ac.be

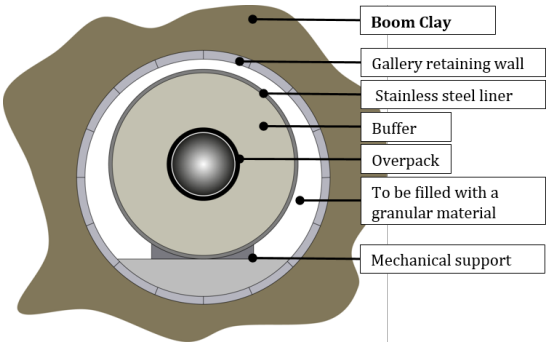

Figure 1. Multi-barriers principle [5]

geochemical environment to prevent corrosion of the containers, and a thermal conductivity that allows enough heat dissipation.

1.2. Scope of the study

Within this framework, in Belgium, Boom Clay is considered [6] as a host formation for deep geological storage. It presents a very low water conductivity and a high radionuclides retention capacity making it a good candidate. An Underground Research Facility (URF) has been built in the north of the country, near Mol [7].

Given the importance of insuring good sealing conditions, the potential host rock - Boom clay - response to the stresses induced by the excavation of the tunnels and the storage of high activity waste has already been thoroughly studied [6][8][9][10]. But during the operation phase the ventilation needed is inducing a variation of the air temperature and relative humidity. These changes lead to the desiccation of the host rock. For this reason, the study of the drying behavior of Boom clay is relevant and an important tool in determining the risk of cracking and potential loss of sealing properties.

1.3. Introduction to the drying kinetics

Drying is an interaction between the porous medium and the atmosphere, and has been studied experimentally using either saline solutions [11] or convective dryers [12]. The latter reproduces natural drying conditions and the analysis of the results gives us a better understanding of the multi-physics processes that occur at the medium surface. This analysis is made in the framework of the boundary layer model (see section 5.1).

The drying kinetics can be analyzed based on weight measurements during the drying process. Three curves can be used: mass loss vs. drying time (Figure 2(a)), drying rate (it is actually a flux since it is per surface area) vs. time (Figure 2(b)) and drying rate vs. water content (Figure 2(c)), called Krischer curve [13]. Krischer curve is used because it gives a clearer picture of the drying kinetics of materials [14, 12].

Krischer curve is studied in parallel with the changes in temperature (Figure 2(d)) at the surface of the sample. The behavior observed in the case where the drying air temperature is significantly higher than the sample initial temperature [15] is visible in Figure 2(d). This was also measured experimentally by Musielak and Jacek [16].

Based on those curves, three periods can be observed [17]:

- I : Preheating Period
- II : Constant Rate Period (CRP)
- III : Falling Rate Period (FRP)

DOI: 10.1002/nag

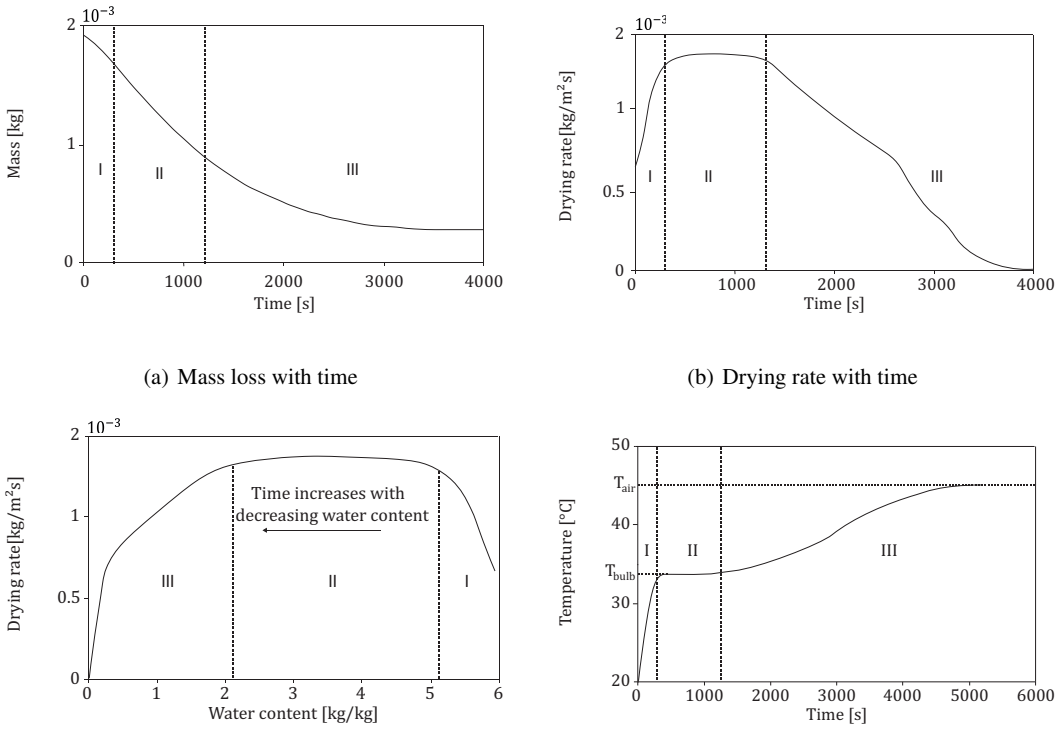

(a) Mass loss with time

(b) Drying rate with time

(c) Drying rate with moisture content

(d) Temperature evolution with time

Figure 2. Drying kinetics

Preheating period The first phase is very short and corresponds to an increase in drying rate. The temperature at the surface of the sample increases from its initial value to the temperature of the wet bulb [15].

Constant Rate Period (CRP) The drying rate reaches a plateau that characterizes the CRP. The heat from the air is completely used for the evaporation of the liquid water at the surface of the sample, the temperature therefore remains constant and equal to the temperature of the wet bulb. The evaporation occurs in a saturated boundary layer. The vapor and the heat transfers are only influenced by the external conditions, i.e. the drying temperature and the air velocity [18, 19]. This period will last until the sample is no longer saturated and internal transfers start to influence the drying rate.

Falling Rate Period (FRP) The FRP is characterized by an increase in the dried body temperature from the wet bulb temperature to the drying air temperature. The drying rate decreases because of the decrease in permeability with the desaturation of the medium.

1.4. Layout of the paper

This paper aims at better understanding the drying behavior of Boom clay through numerical modeling. First, an experimental campaign was conducted [1]. Its protocol is briefly described in section 2. The method used to analyse the tomographic images is explained in section 3. The reconstructions are used to obtain accurate measurements of the samples cross sections. The results are presented in section 4.In sections 5 and 6, a fully coupled thermo-hydro-mechanical framework for unsaturated porous media is introduced and the different sub-models and their

DOI: 10.1002/nag

respective parameters are detailed. The suggested model is used to reproduce the behavior observed experimentally in section 7. And finally, a sensitivity study on the drying parameters, described in section 8, provides insight into the physics behind the drying behavior.

2. EXPERIMENTAL CAMPAIGN

Convective drying tests were performed on Boom clay samples. The experiment is briefly described. Details are available in Prime *et al* [1].

2.1. Studied material

Boom clay is a rock formation located beneath the Mol-Dessel nuclear zone (north-east of Belgium). Its properties make it one of the formation potentially suitable for deep geological nuclear waste disposal [20], as explained in section 1.1.

Boom clay has been the subject of numerous experimental studies in the past 30 years, such as Baldi *et al* [21], Bernier *et al* [6], Chen *et al* [22], Dehandschutter *et al* [9], Horseman *et al* [10], Sultan *et al* [23],etc. They were mainly aimed at characterizing the geological and geotechnical properties of Boom clay to better understand its thermo-hydro-mechanical behavior. Based on the results obtained by those studies in the last decades, Boom clay is considered as a plastic, moderately over-consolidated clay. Wemaere *et al* [24], Aertsens *et al* [25] and Blümling *et al* [26] have shown that it presents a strong anisotropy induced by the clay structure (horizontal bedding with alternaning clay and silt layers) . The thermo-hydro-mechanical properties of Boom Clay are already well documented and a good review can be found in the works of Dizier [8].

2.2. Sample preparation

Cylindrical samples around 35 mm in diameter and in height were water-drilled from the cores (Figure 3(a)) received from the Mol laboratory. The drilling was made parallel to the bedding direction to allow for a faster saturation process. Smaller samples were taken from the cores to determine the water retention curve.

(a) Initial Core from the Mol laboratory

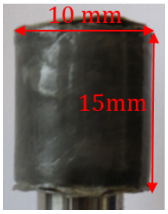

(b) Final samples coated with paraffin

Figure 3. Samples preparation

These were placed in a triaxial cell to saturate them under *in situ* conditions. Since the saturation is a time consuming process, it was necessary to optimize the use of the saturated samples to perform a sufficient number of drying tests to insure repeatability. The saturated samples were divided into smaller cylinders 5, 10 and 15 mm high. Those smaller cylinders were then cut in four quarters from which a 15 mm diameter cylinder is extracted. So from a single saturated sample, twelve smaller cylindrical samples are obtained. Finally, the samples were weighed and dipped in two paraffin baths: a warm bath to ensure good adherence between paraffin and sample, and a colder one to obtain a thick enough layer for efficient sealing (Figure 3(b)). The finished products were stored into a desiccator saturated with water. The entire process was done as quickly as possible to minimize drying prior to the experiments.

DOI: 10.1002/nag

2.3. *Drying tests*

Twelve samples were dried using a micro-convective dryer designed in the Laboratory of Chemical Engineering of the University of Liège [27] and visible in Figure 4 (a)). The dryer is suited for drying light samples using a convective air flow with controlled temperature and velocity. The samples are named using the following method : sample height in millimeters followed by the sample number (e.g. 5-1 for the first 5 mm high sample).

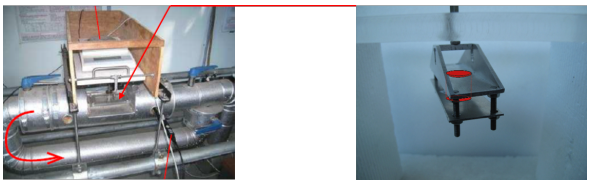

(a) (b)

Figure 4. Convective dryer and sample holder

The paraffin on the top surface of the samples is removed to constrain the drying to only one side. They are then placed vertically in an homemade holder in the drier (Figure 4 (b)), and subjected to a convective air flow of 0.8 m/s at 25°C, and with a relative humidity of around 3.5%. The air flow was kept as parallel as possible to the drying surface to reproduce as closely as possible *in situ* conditions.

2.4. *Data acquisitions*

The sample holder is attached to a scale, allowing to weigh the sample every 30 seconds during the test.

Furthermore, X-ray microtomography was used to scan the samples beforehand and then every hour for four hours, and once more at the end of the drying test. For the tomographic acquisitions the samples had to be removed from the dryer, they were sealed immediately after the removal and during the scan, before returning in the drier. The weighings showed no more than 2 mg variation (0.1 % of the total mass) which is assumed to be linked to the scale precision and the potential evaporation during the scan, and can therefore be neglected.

Acquisitions were made on a Skyscan 1172 from Bruker microCT, at a pixel size of 31.86 or 34.63 µm. The X-ray source was set at 100 kV and a 0.5 mm Aluminium filter was used to harden the beam and limit these artefacts in the reconstructions. For each scan 256 projections were taken, limiting the scanning duration to 6 minutes so as to minimize the impact of the drying interruption. Reconstruction was performed using Bruker's NRecon software, making use of their ring artifact correction, set at a strength of 5.

3. ANALYSIS OF THE TOMOGRAPHIC RECONSTRUCTIONS

Prime presented the results of the convective drying campaign in [27] but further image processing has since been performed, extracting more accurate measurements. Figure 5 shows vertical cross-sections in the tomographic reconstructions of one of the samples, at the saturated state and after 72h of drying. The clay seems relatively homogeneous except for a few small wiry pyrite inclusions that appear as dark discs on the cross-sections, as can be seen in Figure 5(a). Cracks begin to appear fairly rapidly during the drying process, and are clearly visible in Figure 5(b).

To find the cross-sectional area of the samples, a segmentation must first be performed to distinguish the pixels of the samples from the rest. A watershed transformation was performed on the inverse of the image gradient, using as markers for the two regions to separate (clay and air) a low and high threshold of the reconstruction. It is implemented as morphological region-growing algorithm as described in [28]. The gradient was computed with a Sobel mask, and the Euclidean norm was used. Finally, to extract the sample outer boundary, a simple method combined

DOI: 10.1002/nag

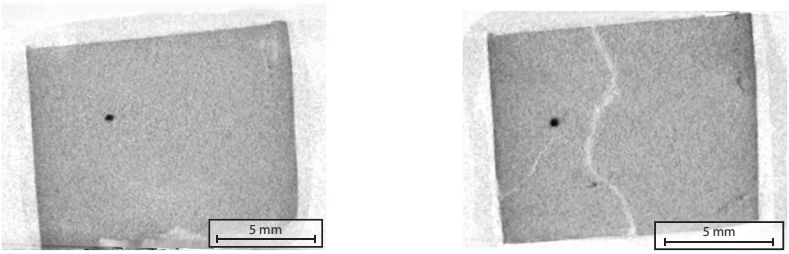

(a) Saturated (b) Dry

Figure 5. Vertical cross-sections in sample 10-1, at roughly the same location, before and after complete drying

connected component analysis, distance transforms, and thresholding. The drying rate, is inversely proportional to the evaporation surface. A good approximating lower bound of this surface can be defined, using the result of the previous procedure, as a horizontal cross-section right below the sample surface, as shown in Figure 6.

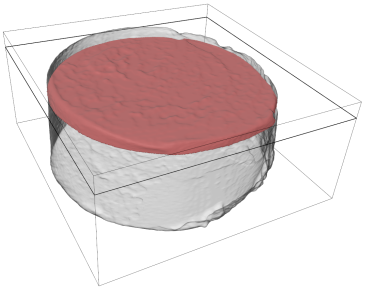

Figure 6. Illustration of the determination of the evaporation surface on sample 5-2 before drying. The transparent grey surface shows the outer interface of the sample, the red cross-section indicating the surface used to approximate the evaporation surface. The thick black frame indicating the height at which the cross-section was taken.

We observe that the shrinkage is orthotropic and relative to the bedding plane orientation, and is taken into account in the mechanical part of the proposed model. The samples were prepared in such a way to have these bedding planes in a vertical position. Therefore the two shrinkage measures needed, parallel and normal to the bedding plane, can be determined by measuring the evolution of the radius of the cylindrical sample in two perpendicular directions.

Contrary to the measure of cross-sectional surface area, radius measurement is much more sensitive to small variations in sample geometry, therefore special care was taken to define where the radius is measured and over what area to average the measure, in order to smooth out local variations.

The methodology is based on previous works focused on 3D registration [29]. To define a radius in a cylindrical sample, a approximating cylinder is first determined, by finding a series of enclosing circle on every axial cross-section [30], and performing a linear regression on the circle centers to find the cylinder axis. This axis is used to transform the coordinate system on the sample interface points from Cartesian to cylindrical, i.e. in the form (h, r, α), where h is the height along the axis (the origin is chosen arbitrarily), r is the distance from the axis, and α is the angle around it. As a convention, we chose an angle of 0 to be parallel to the bedding plane. The plane direction was set by manual observation of the images, locating the crack directions. As no cracks appear in the saturated samples, we used other features visible in the tomographic reconstructions, such as the pyrite inclusions, and related those to the cracks in the images after drying. The set of interface points (Figure 7(a)) in cylindrical coordinates is then decomposed into 2 subsets based on height

DOI: 10.1002/nag

and angle. We chose to study the interface points in the middle vertical portion of the sample in the range of $h = \pm 50$ pixels around the median. For the measurements in the two perpendicular directions, we chose angular wedge of $45°$ around $0°$ and $180°$ for the parallel measurements, and $90°$ and $270°$ for the perpendicular one (Figure 7(b)). These two subsets contain on average 15000 points, which gives a good representativity. Finally, in each subset the average radius is determined, and if we call r_0 and r_∞ this average radius at the saturated stage and at the dry stage respectively, then the shrinkage will equal $1 - \frac{r_\infty}{r_0}$.

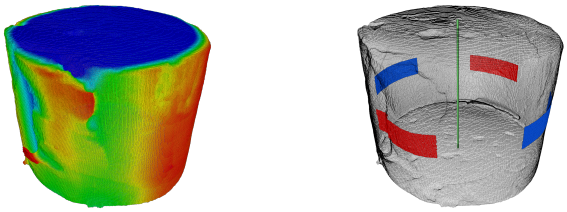

(a) (b)

Figure 7. Illustration of the radius measurements on sample 10-1. (a) shows the interface points colored by radius, the colormap, from blue to red, is centered around the average radius. (b) shows the two subsets, colored in red and blue, used for the determination of the perpendicular and parallel radii.

4. EXPERIMENTAL RESULTS

Prime presented the results of the convective drying campaign in [1] but based on the same data acquisition the image processing has changed as described in 3 and was improved upon with help from the department of Chemical Engineering from the University of Liège. The goal was to have a more consistent approach to obtain more accurate surface results. The main challenges to overcome were to precisely take into account the axial shrinkage and the initial out-of-plumb (or straightness default).

From the constant weighing of the samples during the drying process, drying kinetics can be determined. The shrinkage profile is obtained using the surface area measurement based on the cross-sections of the reconstructions. For now, the results from samples 5-1, 5-2 and 5-4 were used to validate the model.

4.1. Drying kinetics

Mass as a function of drying time is plotted in Figure 8 and shows that the dry state is reached after around 10 h with intense mass loss during the first 2 or 3 hours of the test.

The drying rate can be calculated based on the mass loss and the evaporation surface:

$$q = -\frac{1}{S}\frac{dm}{dt} \tag{1}$$

where m $[g]$ and S $[m^2]$ are respectively the measured mass and top surface of the sample.

Since clay undergoes shrinkage during drying, the surface area changes for the drying rates at different times of the drying. This changes was measured using the measures of cross-sectional area from the tomographic reconstructions (see Fig. 6).

This drying rate can then be plotted as a function of time or used for plotting the Krischer curve. The drying rate presents heavy fluctuations when the raw data from the weight measurements are used due to the small time steps between two weighings, during which mass may not vary enough. Consequently, the curves have been smoothed with a Lanczos filter [31]. Using this smoothed data, drying rate evolution and Krischer curves for the three studied samples are shown in Figure 9 and

DOI: 10.1002/nag

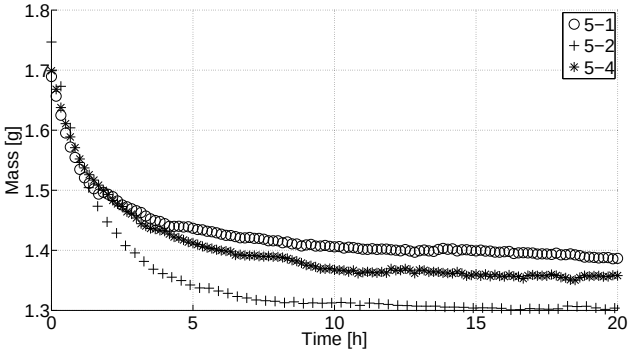

Figure 8. Observed mass loss for the three 5 mm high samples

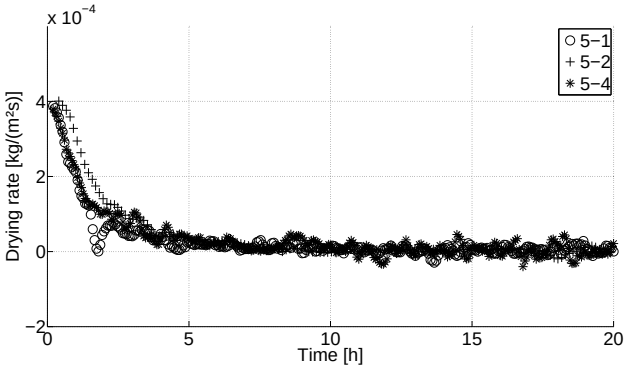

Figure 9. Observed drying rate for the three 5mm high samples

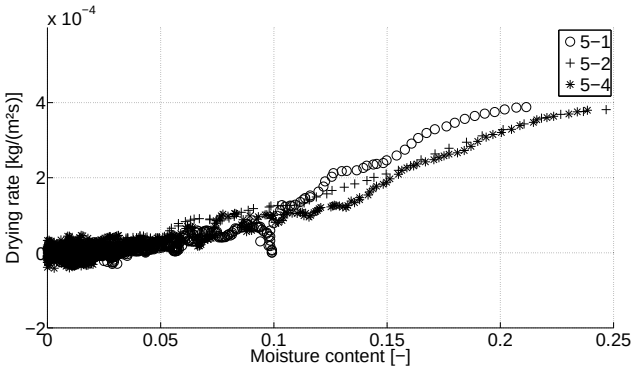

Figure 10. Observed Krischer curve for the three 5mm high samples

Figure 10 respectively. The first thing that should be noted is that the water content is continuous, confirming our assumption that the evaporation of water during the scanning could be neglected.

Contrary to the theoretical curve, there is little to no CRP. This can be explained using Lehmann's theory [32]. His studies aimed at characterizing an hydraulic connection layer between the evaporation surface and the drying front. This connection layer has been shown to be necessary to observe a constant drying rate [33]. The assumption is made that the length of the connection layer corresponds to the equilibrium of gravitational, capillary and viscous effects :

$$\Delta h_{cap} = \Delta h_{visc} + \Delta h_{grav} \tag{2}$$

with Δh_i corresponding respectively to the capillary, viscous and gravitational hydraulic heads.

DOI: 10.1002/nag

Capillary effects depends on the microstructure of the porous medium. Lemhann [32] suggests using the slope of the tangent to the water retention curve at the inflection point to express the capillary hydraulic head :

$$\Delta h_{cap} = \frac{\alpha_{vG}}{(n_{vG}-1)} \left(\frac{(2n_{vG}-1)}{n_{vG}} \right)^{\left(\frac{(2n_{vG}-1)}{n_{vG}}\right)} \left(\frac{(n_{vG}-1)}{n_{vG}} \right)^{\left(\frac{(1-n_{vG})}{n_{vG}}\right)} \tag{3}$$

with α_{vG} $[Pa]$ and n_{vG} $[-]$ are van Genuchten's model parameters.

Viscous head loss is proportional to the flow velocity and Darcy's law for unsaturated porous medium is used to determine Δh_{visc} :

$$\Delta h_{visc} = \frac{L_{crit} q_{max}}{k_{rel,w}(S_{r,w}) k_{sat} \rho_w} \tag{4}$$

It depends on the depth of the drying front, L_{crit} $[m]$, the maximal drying rate, q_{max} $[kg/m^2/s]$ and the water permeability, $k_{rel,w}(S_{r,w})k_{sat}$ $[m/s]$. It is assumed that the water content decreases linearly from the drying front to the drying surface and the mean permeability between those two points is used to determine viscous resistance [32]. The gravitational head loss is directly linked to the length of the connection layer and is expressed :

$$\Delta h_{grav} = L_{crit} \tag{5}$$

Now, substituting equations 3-5 in equation 2, it gives :

$$L_{crit} = \frac{\Delta h_{cap}}{1 + \frac{q_{max}}{k_{rel,w}(S_{r,w}) k_{sat}}} \tag{6}$$

Based on our experimental results ($q_{max} = 3,8.10^{-4}$ $[kg/m^2/s]$) and our material properties ($k_{sat} = 8.10^{-12}$ $[m/s]$), the value of the critical length is $L_{crit} = 6.01$ mm.

That length is very close to our sample size and so a CRP is initially possible. But as soon as the sample desaturates, the permeability decreases inducing a smaller critical length and the loss of the liquid connection between the evaporation surface and the drying front and thus the end of the CRP. This explains why a very short CRP is observed since the smallest drop in permeability means the end of the CRP. Moreover, the water contents is continuous confirming our assumption that the evaporation of water during the scanning could be neglected.

4.2. Shrinkage

Using the micro-tomographic scans, it is possible to follow the evolution of the cross sections of the sample along its height or to follow the evolution of a chosen cross section (Figure 12). From that evolution, and knowing the bedding direction, the evolution of the radii parallel and perpendicular to the bedding plane can be determined (Figure 11(a) and Figure 11(b)). On both Figure 12 and Figure 11, it can be observed that most of the shrinkage takes place at the very beginning of the drying (around 2/3 of the final strain has developed after 1 hour). Figure 11 also shows that the shrinkage quickly becomes uniform on the sample height. An other information that can be taken from both figures is that the results after 4h are incoherent for sample 5-1. It is especially showing on Figure 11 where the radius increases. This is due to problems with the reconstruction of the tomographic scans.

5. THERMO-HYDRAULIC MODEL

Boom Clay is considered an unsaturated porous medium with a solid, a liquid and a gas phase, as shown in Figure 13. Within this medium, the liquid water transfers are governed by Darcy's law and vapor diffusion is controlled by Fick's law. Evaporation at the surface of the medium and heat transfer are calculated using the boundary layer model.

DOI: 10.1002/nag

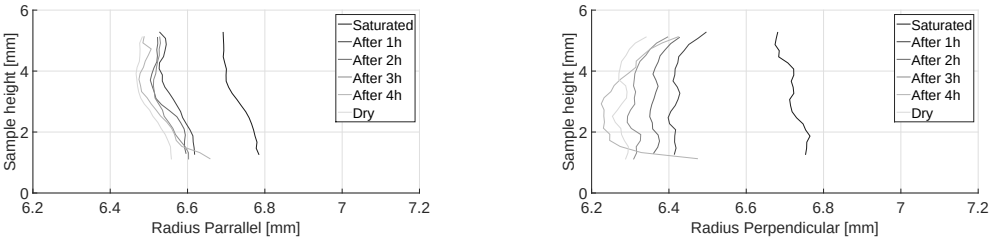

(a) Evolution of the radius parallel to the bedding plane with time

(b) Evolution of the radius perpendicular to the bedding plane with time

Figure 11. Evolution of the radii for sample 5-1

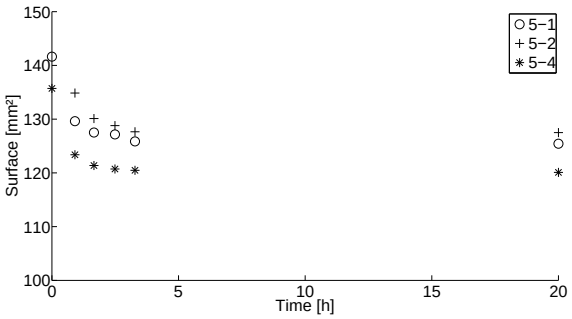

Figure 12. Evolution of the surface of a chosen cross section (top of the sample)

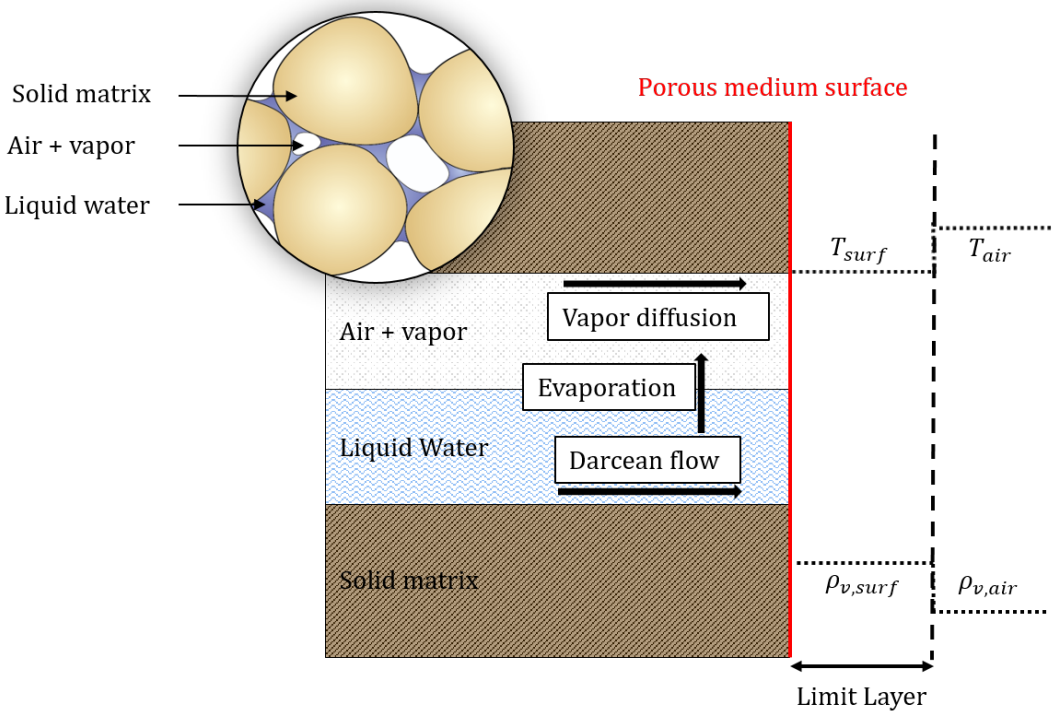

Figure 13. Water transfer mechanism

DOI: 10.1002/nag

5.1. Vapor and heat exchange

The results are analyzed based on the assumption of the existence of a boundary layer all around the sample where the mass and heat transfers are assumed to take place [12]. The water flow, $\bar{q}$, from the materials to the surroundings is assumed to be proportional to the difference between the vapor density of the drying air, $\rho_{v,air}$ $[kg/m^3]$, and at the surface of the sample, $\rho_{v,surf}$ $[kg/m^3]$, [34, 35]. The proportionality coefficient is a mass transfer coefficient, α $[m/s]$, characterizing the surface transfer properties. The water flow is expressed as:

$$\bar{q} = \alpha(\rho_{v,surf} - \rho_{v,air}) \tag{7}$$

The heat flux, $\bar{f}$, from the boundary to the drying air is expressed as:

$$\bar{f} = L\bar{q} - \beta(T_{air} - T_{surf}) \tag{8}$$

where T_{air} $[°C]$ is the temperature of the drying air, T_{surf} $[°C]$ is the temperature at the surface of the sample, β $[W/m^2/K]$ is a heat transfer coefficient and L is water evaporation latent heat (2500 kJ/kg).

Based on the drying kinetics, it is possible to determine the transfer coefficients (Eq. 7 and Eq. 8). The value of the drying rate during the CRP is directly linked to the capacity of the drying air to evaporate the water at the surface of the porous medium, and is therefore linked to the value of the mass transfer coefficient. Hence to determine the value of the transfer coefficient, the value of the drying rate during the CRP is used. The same can be done for the heat transfer, the drying rate during the CRP is used, and the temperature corresponds to the wet bulb temperature which can be analytically determined. No temperature measurements are actually required and only knowing the drying rate is sufficient to determine the heat transfer coefficient.

Samples	Mass transfer α $[m/s]$	Heat transfer β $[W/m^2/K]$
$5-1$	0.047	52.2
$5-2$	0.049	55.2
$5-4$	0.048	53.3

Table I. Transfer coefficients

As can be seen in table I, the mean mass and heat transfer coefficients are around respectively 0.048 $[m/s]$ and 53.5 $[W/m/K]$ with a standard deviation inferior to 10% for all the samples tested [1].

5.2. Water internal transfers

The clay is an unsaturated porous medium, partly saturated by liquid water and gas (air + vapor). The water mass balance equation is based on the Richard's equation :

$$\underbrace{\frac{\partial(\rho_w n S_{r,w})}{\partial t} + div(\rho_w \underline{f}_w)}_{\text{Liquid water}} + \underbrace{\frac{\partial(\rho_v n S_{r,g})}{\partial t} + div(\underline{i}_v + \rho_v \underline{f}_g)}_{\text{Water vapor}} = Q \tag{9}$$

where ρ_w $[kg/m^3]$ and ρ_v $[kg/m^3]$ are respectively the liquid water and the vapor densities, n $[-]$ is the porosity, $S_{r,w}$ $[-]$ and $S_{r,g}$ $[-]$ are respectively the water and the gas saturation degrees in volume, t $[s]$ the time, Q $[kg/s]$ is the injected flux, $\underline{f}_w$ $[m/s]$ and $\underline{f}_g$ $[m/s]$ are the water and gas phase respective macroscopic velocity and $\underline{i}_v$ $[kg/m^2 s]$ is the non-advective flux of water vapor.

Flow Liquid water and gas macroscopic velocity are given, respectively for $i = w, g$ by the generalization of Darcy's law :

DOI: 10.1002/nag

$$\underline{f}_i = -\frac{k_{rel,i}(S_{r,i})\underline{\underline{k}}_{sat}}{\mu_i}(\underline{\nabla} p_i + g\rho_i \underline{\nabla} z) \tag{10}$$

in which, $k_{rel,i}$ $[-]$ is the phase relative permeability, $\underline{\underline{k}}_{sat}$ $[m^2]$ the intrinsic saturated permeability, p_i $[Pa]$ the phase pressure, g $[m/s^2]$ the gravity acceleration, μ_i $[Pa.s]$ the phase viscosity and z $[m]$ is the upwards vertical spatial coordinates. The water relative permeability $k_{rel,w}$ can be determined based on degree of saturation of the phase and the formulation proposed by van Genuchten:

$$k_{rel,w} = \sqrt{S_{r,w}}(1 - (1 - S_{r,w}{}^{\frac{1}{m_{vG}}})^{m_{vG}})^2 \tag{11}$$

where m_{vG} $[-]$ is a model parameter. The retention curve links the phase saturation to the capillary pressure. The formulation proposed by van Genuchten [36] is used in our model:

$$S_{r,w} = S_{res} + (S_{sat} - S_{res})(1 + (\frac{p_c}{\alpha_{vG}})^{n_{vG}})^{-m_{vG}} \tag{12}$$

$$S_{r,g} = 1 - S_{r,w} \tag{13}$$

in which n_{vG} $[-]$, m_{vG} $[-]$ are model parameters, α_{vG} $[Pa]$ is a model parameter related to the air entry pressure, S_{res} $[-]$ is the water residual saturation, S_{sat} $[-]$ is the water maximal saturation and p_c $[Pa]$ is the capillary pressure.

Anisotropic intrinsic permeability The advective flow of water depends on the anisotropy of the material. This is taken into account by introducing an anisotropic intrinsic permeability tensor. However most materials present limited forms of anisotropy and stratified materials require only two parameters for the description of the water flow. For vertical layering , the intrinsic hydraulic permeability tensor is defined by :

$$\underline{\underline{k}}_{sat} = \begin{pmatrix} k_{sat,/\!/} & 0 & 0 \\ 0 & k_{sat,\perp} & 0 \\ 0 & 0 & k_{sat,/\!/} \end{pmatrix} \tag{14}$$

where $k_{sat,/\!/}$ $[m^2]$ and $k_{sat,\perp}$ $[m^2]$ are the intrinsic permeabilities parallel and perpendicular to the layers, respectively.

Vapor diffusion The water vapor flow is assumed to follow Fick's law of diffusion in a tortuous medium. The vapor diffusion is linked to the vapor density gradient:

$$\underline{i_v} = -D_{atm}\tau_v n S_{r,g} \nabla(\rho_v) \tag{15}$$

where D_{atm} $[m^2/s]$ molecular diffusion coefficient and τ_v $[-]$ is the tortuosity. Vapor is assumed to be in equilibrium with liquid water.

5.3. Heat diffusion

To be able to simulate the temperature evolution within the medium, we use the classic governing energy balance equation :

$$\dot{S}_T + div(V_T) - Q_T = 0 \tag{16}$$

where $\dot{S}_T$ is the heat storage, V_T is the heat flux and Q_T is the heat production term. In the derived balance equation 16, the heat storage term can be expressed as follows:

$$\begin{aligned} S_T = nS_{r,w}\rho_w c_{p,w}(T - T_0) + nS_{r,g}\rho_a c_{p,a}(T - T_0) + \\ (1 - n)\rho_s c_{p,s}(T - T_0) + nS_{r,g}\rho_v c_{p,v}(T - T_0) + LnS_{w,g}\rho_v \end{aligned} \tag{17}$$

DOI: 10.1002/nag

in which, $c_{p,w}$, $c_{p,a}$, $c_{p,s}$ and $c_{p,v}$ are respectively the water, the air, the solid and the vapor specific heats $[J/kgK]$, ρ_w, ρ_a, ρ_s and ρ_v are respectively the water, the air, the solid and the vapor densities $[kg/m^3]$. The heat flux consists of a conduction term proportional to the thermal conductivity of the porous medium and a convective term related to the heat transported by fluid flows:

$$V_T = -\Gamma\nabla T + c_{p,w}\rho_w \underline{f}_w(T-T_0) + c_{p,a}\rho_a \underline{f}_g(T-T_0) + c_{p,v}(\rho_v \underline{f}_g + \underline{i}_v)(T-T_0) + (\rho_v \underline{f}_g + \underline{i}_v)L \quad (18)$$

where Γ $[W/mK]$ is the porous medium thermal conductivity, T_0 $[K]$ is the initial temperature and T $[K]$ is the temperature.

6. MECHANICAL MODEL

Boom clay is a overconsolidated plastic clay ($p_0 = 6[MPa]$ [37]). Most of the time in the literature, its behavior has been modeled using isotropic CamClay ([38] [39]). More recently, T-H-M experiments in the URF at Mol exhibited Boom Clay's anisotropy [8]. These experiments were modeled using transverse isotropic model [22]. The drying experiments conducted on Boom clay also displayed that anisotropy (cf. section 4). But during a drying experiment, loading and boundary conditions lead to an almost isotropic stress path with stresses staying below p_0. For these reasons, we suggest to use an elastic orthotropic model to simulate the drying experiments. Classically, a couple of stresses (net stress and suction [40] is used to reproduce plastic collapse during wetting path. Nonetheless, for drying path, the effective stress allows to reproduce the observed behavior.Bishop's effective stress has been chosen to describe the stress-strain relation because it directly incorporates the effect of the suction. It is expressed as:

$$\sigma'_{ij} = \sigma_{ij} - p_g\delta_{ij} + S_{r,w}(p_g - p_w)\delta_{ij} \quad (19)$$

where σ'_{ij} $[Pa]$ is the effective stress tensor, σ_{ij} $[Pa]$ is the total stress tensor, $S_{r,w}$ $[-]$ is the water saturation and δ_{ij} is Kronecker's tensor. p_g and p_w denote respectively gas and water pressure $[Pa]$. The strain is related to the effective stress through the following relation :

$$\epsilon_{ij} = D^e_{ijkl}\sigma'_{ij} \quad (20)$$

where σ'_{ij} is the elastic stress tensor and ϵ_{ij} is the elastic strain and D^e_{ijkl} is the elastic compliance tensor defined as:

$$D^e_{ijkl} = \begin{bmatrix} \frac{1}{E_{/\!/}} & -\frac{\nu_{\perp,/\!/}}{E_\perp} & -\frac{\nu_{z,/\!/}}{E_z} & 0 & 0 & 0 \\ -\frac{\nu_{/\!/,\perp}}{E_{/\!/}} & \frac{1}{E_\perp} & -\frac{\nu_{z,\perp}}{E_z} & 0 & 0 & 0 \\ -\frac{\nu_{/\!/,z}}{E_{/\!/}} & -\frac{\nu_{\perp,z}}{E_\perp} & \frac{1}{E_z} & 0 & 0 & 0 \\ 0 & 0 & 0 & \frac{1}{2G_{/\!/,\perp}} & 0 & 0 \\ 0 & 0 & 0 & 0 & \frac{1}{2G_{/\!/,z}} & 0 \\ 0 & 0 & 0 & 0 & 0 & \frac{1}{2G_{\perp,z}} \end{bmatrix} \quad (21)$$

The symmetry of the stiffness matrix imposes that:

$$\frac{\nu_{\perp,/\!/}}{E_\perp} = \frac{\nu_{/\!/,\perp}}{E_{/\!/}}, \frac{\nu_{z,/\!/}}{E_z} = \frac{\nu_{/\!/,z}}{E_{/\!/}}, \frac{\nu_{\perp,z}}{E_\perp} = \frac{\nu_{z,\perp}}{E_z} \quad (22)$$

Where E_i $[MPa]$ is Young's modulus and ν_i is Poisson's ratio with the indice *i* representing the diffent directions considered. $/\!/$ refers to the radial direction parallel to the bedding plane. $\perp$ refers to the radial direction perpendicular to the bedding plane and z to the axial direction of the cylinder. The axial direction is also parallel to the bedding plane but due to slightly different values of the

DOI: 10.1002/nag

shrinkage (cf. Figure 21, a different elastic modulus is used. Hence, the use of an orthotropic model and not a transverse isotropic one.

In the previous equations, elastic modulus are not constant but depends on the stress state. We suggest to use a non linear elasticity law used based on the formulation of Modaressi and Laloui [41] :

$$E_i = E_{0,i} + E_{ref,i}(\frac{p'}{p_{ref}})^b \tag{23}$$

where E_{ref} is the increment of the Young modulus at the reference mean effective stress, p_{ref} and b is a model parameter. $E_{0,i}$ is used to avoid null Young's modulus when the effective stress state vanishes.

It has to be noted that while cracking is experimentally observed, no tensile strength criterion is included because Boom Clay presents very clear bedding planes which were experimentally proved to be the cause of cracks initiation. It would thus be better suited to use initial defaults at the level of the bedding planes and work in a crack propagation framework based on required energy or crack toughness. Another possible method would be to calibrate a cohesive interface mechanism.

7. NUMERICAL RESULTS AND VALIDATION

In this section, the model introduced in section 5 - 6 is used to reproduce the drying behavior of the Boom Clay samples tested during the experimental campaign (cf. section 2). Values for the different parameters are given. As shown in section 4, variability between samples is low and their behavior is very similar because the hydraulic connection layer is shorter than the height of any of the samples experimentally tested. Therefore using only one sample to perform the model validation is acceptable. Sample 5-1 was arbitrarily chosen. The study was conducted using the finite element code LAGAMINE developped at the university of Liège [42].

Drying kinetics

Figure 14, Figure 15, and Figure 16, which present mass loss, drying rate, and Krisher's curve, all show a good fit with the experimental results, confirming the ability of the suggested model to represent the drying behavior of this porous unsaturated material, despite the numerical problems inherent to the calculation of water flows in low permeability drying materials.

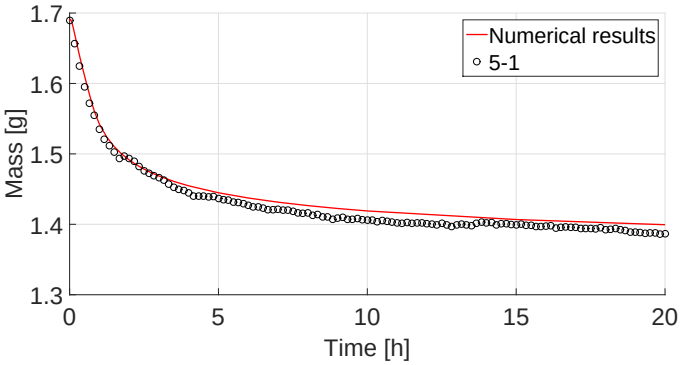

Figure 14. Comparison of experimental and numerical mass loss for sample 5-1

The values of the water permeability are not directly extracted from Bernier *et al* [6] but are in accordance with the range suggested (table II).

DOI: 10.1002/nag

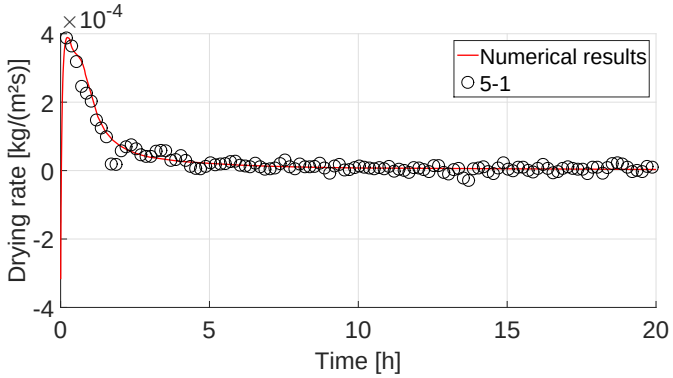

Figure 15. Comparison of experimental and numerical drying rate evolution with time for sample 5-1

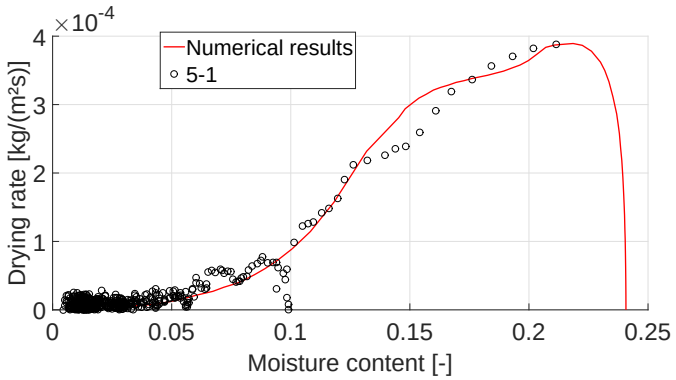

Figure 16. Comparison of experimental and numerical Krisher's curve for sample 5-1

References	Parameters	Values	Units
Hydraulic parameters			
	$k_{sat,/\!/}$	6.10^{-19}	$[m^2]$
	$k_{sat,\perp}$	3.10^{-19}	$[m^2]$
	n	0.39	$[-]$
van Genuchten parameters			
Prime *et al* [1]	α_{vG_w}	15	$[MPa]$
	n_{vG_w}	1.7	$[-]$
	S_{sat}	1	$[-]$
	S_{res}	0.01	$[-]$

Table II. Hydraulic model parameters

Temperature

Since the temperature of the sample was not recorded during the drying test, validation of the numerical results is not possible. They are however presented in Figure 17. The temperature decreases from its initial value of $17°C$ (temperature of the room) to a minimum around $8°C$. This is logical since the drying air temperature ($25°C$) is not very high and therefore cannot provide sufficient heat to enable the evaporation on its own. Heat from the porous medium is used and the temperature of the sample decreases until it reaches the temperature of the wet bulb. No constant temperature period is observed since we have no CRP. As explained in section 1.3, the temperature remains at a constant value equal to the wet bulb temperature if and only if there is a CRP. When

DOI: 10.1002/nag

the drying rate decreases, the evaporation process is less intense and the heat supply is more than the quantity needed for the evaporation, so the temperature of the sample increases until it reaches the temperature of the drying air. The parameters used are shown in table III.

References	Parameters	Values	Units
	ρ_w	1000	$[kg/m^3]$
	$c_{p,w}$	4185	$[J/kg/K]$
	ρ_a	1.2	$[kg/m^3]$
	$c_{p,a}$	1004	$[J/kg/K]$
	ρ_v	0.59	$[kg/m^3]$
	$c_{p,v}$	1864	$[J/kg/K]$
Bernier *et al* [6]	ρ_s	2670	$[kg/m^3]$
Wouters and Vanderberghe [43]	$c_{p,s}$	1400	$[J/kg/K]$

Table III. Thermal model parameters

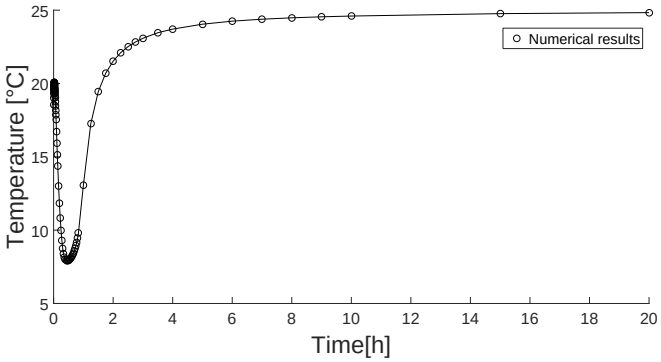

Figure 17. Numerical variation of the temperature with time at the drying surface

Shrinkage

Figure 18 shows the variation of a chosen cross section (1mm under the drying surface) of the sample with time. Non linear elasticity allows to reproduce the material stiffening and lead to a good fit of the experimental results.

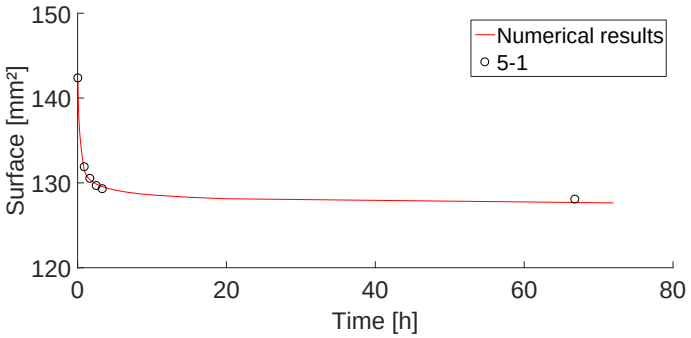

Figure 18. Comparison of experimental and numerical surface with time

Figure 19 shows the evolution of the radii parallel and perpendicular to the bedding plane at different time steps. The results are expressed as a ratio of the original radius to avoid surface

DOI: 10.1002/nag

effects linked to the original shape of the sample (cf. Figure 11 in section 4). As can be seen the fit is also good with errors never exceeding 2%. The differences that can be seen around the top and the bottom of the sample are caused by the non parallelism of the external surfaces but also by damages done to the samples while preparing them. This means that the extremities of the sample are very uneven and measurements inconsistent.

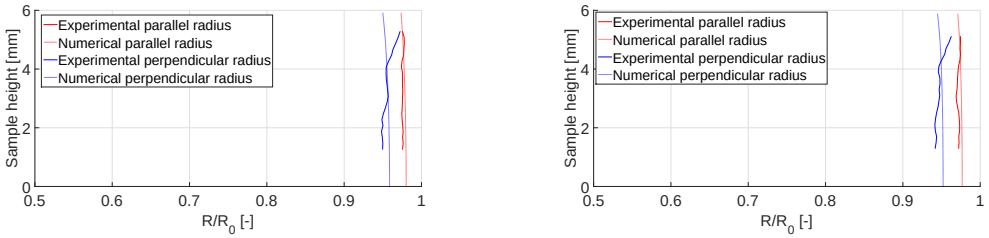

(a) After 1h of drying

(b) After 2h of drying

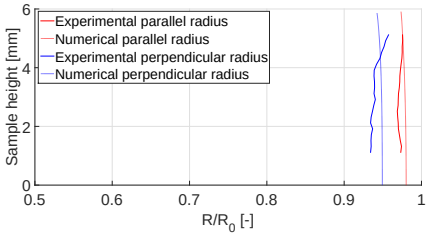

(c) After 3h of drying

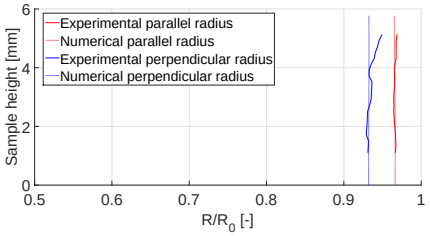

(d) Dried samples

Figure 19. Evolution of the radii for sample 5-1 at different times

Volume is not as accurately estimated because of the accumulated error on the different sections along the sample height. Nonetheless, the numerical results are still close to the experimental value with errors inferior to 2% as visible on Figure 20.

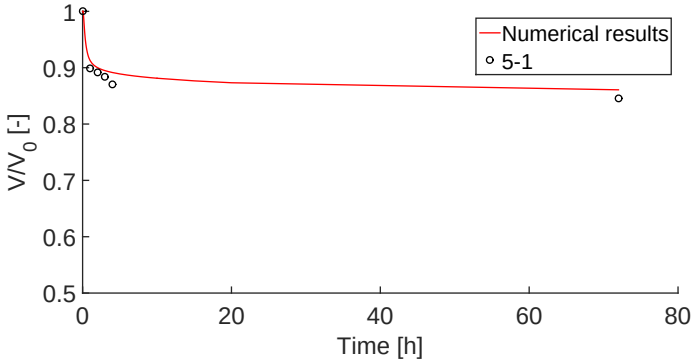

Figure 20. Comparison of experimental and numerical volume evolution with time

Figure 21 shows the final shrinkage in all the principal directions, averaged over the tested samples. We note that the simulated shrinkage is very close to the experiment, in all directions. This was made possible using an orthotropic mechanical law.

The mechanical parameters used are presented in table IV. A ratio $\frac{E_{/\!/}}{E_{\perp}} = 2$ is used which is in accordance with studies on the transverse anisotropy of overconsolidated clay [44, 45] and this range of value was already used for Boom clay in the work of Dizier[8]. The value used for E_z, ref is based on retro fitting done on the final value of the axial shrinkage shown in Figure 21. This was

DOI: 10.1002/nag

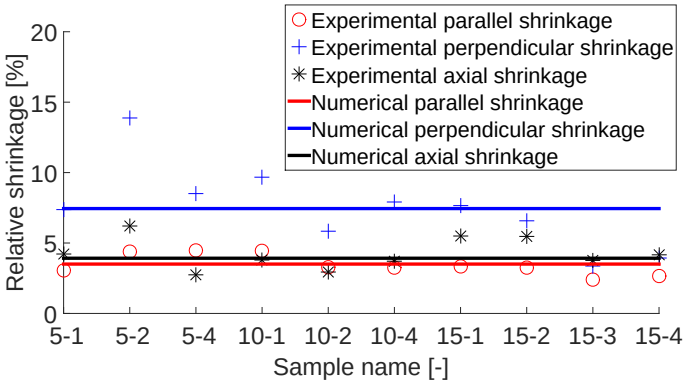

Figure 21. Comparison between numerical and experimental shrinkage values for all the samples tested

References	Parameters	Values	Units
Dizier[8]	$\nu_{/\!/,\perp}$	0.125	$[-]$
	$\nu_{/\!/,z}$	0.0625	$[-]$
	$\nu_{\perp,z}$	0.0625	$[-]$
	$G_{\perp,/\!/}$	140	$[MPa]$
	$G_{\perp,z}$	140	$[MPa]$
	$E_{/\!/,ref}$	350	$[MPa]$
	$E_{\perp,ref}$	175	$[MPa]$
	$E_{z,ref}$	300	$[MPa]$
	b	0.8	$[-]$

Table IV. Mechanical model parameters

necessary since the observed axial shrinkage is higher then the shrinkage parallel to the bedding plane.

8. SENSITIVITY STUDY

The goal of this section is to get a better understanding of the physics behind the coupled model through a sensitivity study.

First, the influence of water permeability is analyzed to show when internal transfers govern or not the drying process. Then, the influence of water retention and water permeability curves is investigated. Finally, the influence of Young's modulus is studied.

8.1. Permeability

The permeability of the porous medium is a key parameter controlling the drying kinetics. Indeed, if the permeability is important enough, the water will easily reach the surface and the drying rate will be governed by the capacity of the drying air to evaporate the water at the surface of the porous medium. On the contrary, if the permeability is very low, the drying rate will quickly drop after the evaporation of the water at or very near the surface because of the time the rest of the water will need to reach that evaporating surface. Using the notion of connection layer [32] introduced in section 4, several values of permeability are chosen to perform this sensitivity study. Knowing the maximum drying rate and the capillary hydraulic head in equation 6, it is possible to determine the water permeability of the medium to get a chosen connection layer length. We decided to use critical lengths equal to 10000 times, 10 times, 1 time and 1 tenth of the sample length. It gives respectively intrinsic permeability of 8.10^{-15} $[m^2]$, 8.10^{-18} $[m^2]$, 8.10^{-19} $[m^2]$ and 8.10^{-20} $[m^2]$.

DOI: 10.1002/nag

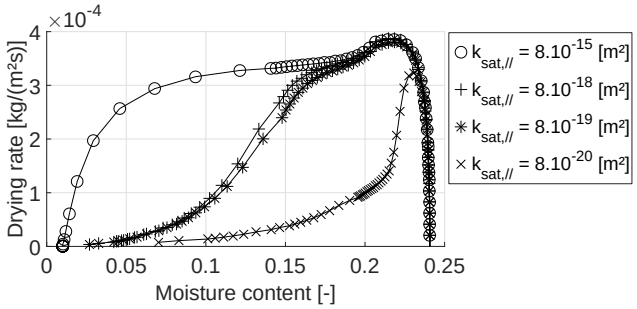

Figure 22. Sensitivity to the water permeability of the porous medium

Figure 22 shows the different drying rates obtained with the different intrinsic permeability chosen. As can be seen, the behavior for. For $k_{sat,//} = 8.10^{-15}\ [m^2]$, a long CRP is observable which is linked to the fact that the permeability has to decrease a lot before the critical length becomes smaller than the sample size and the CRP ends since the critical length is much higher than the sample length. For the $k_{sat,//} = 8.10^{-18}\ [m^2]$ curve or $k_{sat,//} = 8.10^{-19}\ [m^2]$, the CRP is limited as explained in section 4. Finally, the $k_{sat,//} = 8.10^{-20}\ [m^2]$ curve presents no CRP at all since the critical length is initially smaller than the sample size and no CRP is thus possible. That kind of behavior can be observed experimentally with material presenting very different permeabilities as seen in Figure 23.

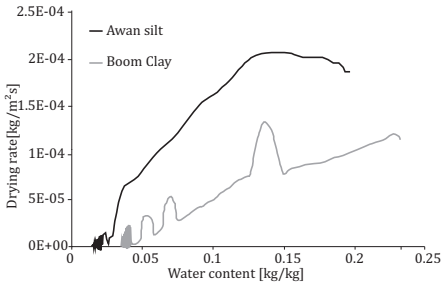

Figure 23. Experimental drying rate for silty material and for clayey material [46]

The following simulations are based on an intrinsic permeability of $k_{sat,//} = 8.10^{-15}\ [m^2]$. This value was chosen since it allows for a well defined CRP which is useful to more clearly exhibit the effects of other parameters.

8.2. Retention curve

Figure 24(a) shows the drying kinetics for different water retention curves. They differ by the value of the α_{vG} parameter in van Genuchten's formulation (Eq.13), which is directly correlated to the air entry pressure. When α_{vG} is high, the porous medium remains saturated for higher suction values. The drying rate is therefore lower since very little water is allowed to leave the medium before the suction reaches high values. Then the drying rate decreases slowly due to the quantity of water still to be evaporated and the permeability still being quite high. On the other hand, when α_{vG} is low, the water inside the porous medium becomes quickly available leading to a higher drying rate but steeper decrease due to the low quantity of water left.

8.3. Young's modulus

Young's modulus mostly affects the shrinkage of the drying surface. The lower the modulus, the more shrinkage there is and thus the smaller the drying surface. This leads to a higher drying rate

DOI: 10.1002/nag

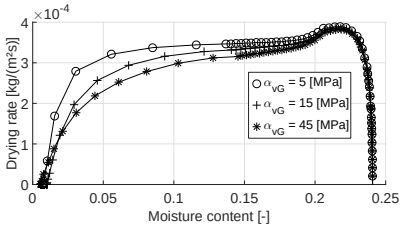

(a) Krischer's curve

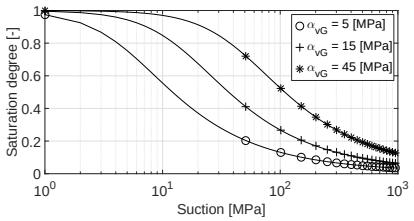

(b) Water Retention Curve

Figure 24. Sensitivity to the water retention curve chosen

(Figure 25) since the surface term is smaller in Eq. 1. The second effect of a low modulus is that the deformation of the porous medium follows exactly the mass loss so that the sample remains saturated for much higher suction values. This leads to higher permeability and thus higher drying rates.

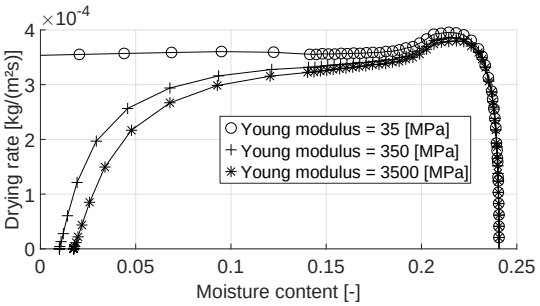

Figure 25. Sensitivity to the Young modulus

9. CONCLUSION

This paper has presented the formulation of a thermo-hydro-mechanical model for studying the drying behavior of Boom clay. The main focus of this study was to validate the capacity of the model to closely match the drying experiments conducted. We first introduced these experiments [1]. Some detailed explanations on the acquisition and processing of the experimental data are also given in section 2 and 3. X-ray microtomography is used to scan the samples and 3D image processing is used to quantify structure evolution. The hydraulic model is based on Richards equation for water flow in unsaturated soils using van Genuchten's formulation to determine the saturation degree and relative permeability. The thermal model is a classical energy balance equation. The mechanical model is an elastic orthotropic model with non linear elasticity expressed in Bishops effective stress. Numerical simulations were conducted in order to show the performance of the proposed model. Comparison with experimental results showed that the model is capable of closely reproducing the observed behavior. Finally, a sensitivity analysis was performed on the water retention curve, permeability and Young's modulus to get a better understanding of the physics behind the suggested model. Further work can be done to improve on this model, namely to consider cracking that may occur during the drying process and its effect on the drying kinetics. Since Boom clay presents a clear bedding, if cracking occurs, it will occur alongside the bedding planes, being a "weakness" in the medium structure. To represent that behavior, a suggested solution is to use interface finite elements to reproduce crack propagation and use experimental data to validate it [47].

REFERENCES

DOI: 10.1002/nag

1. Prime N, Levasseur S, Miny L, Charlier R, Léonard A, Collin F. Drying-induced shrinkage of boom clay: an experimental investigation. *Canadian Geotechnical Journal* 2015; **52**(999):1–14.
2. Belgium Profile. Radioactive waste management programms in oecd/nea member countries. *Technical Report*, Nuclear energy agency 2013.
3. NEA. Moving forward with geological disposal of radioactive waste, a collective statement by the nea radioactive waste management commitee (rwmc). *Technical Report*, OECD-Nuclear Energy Agency, Paris 2008.
4. IEAA. Scientific and technical basis for the geological disposal of radioactive wastes. *Technical Report*, International Atomic Energy Agency, Viena 2003.
5. Craeye B, De Schutter G, Van Humbeeck H, Van Cotthem A. Early age behaviour of concrete supercontainers for radioactive waste disposal. *Nuclear Engineering and Design* 2009; **239**(1):23–35.
6. Bernier F, Li XL, Bastiaens W. Twenty-five years' geotechnical observation and testing in the tertiary boom clay formation. *Géotechnique* 2007; **57**(2):229–237.
7. Bastiaens W, Bernier F, Buyens M, Demarche M, Li XL, Linotte JM, , Verstricht J. The connecting gallery. *Technical Report*, EURIDICE 2003.
8. Dizier A. Caractérisation des effets de température dans la zone endommagée autour de tunnels de stockage de déchets nucléaires dans des roches argileuses. PhD Thesis, Université de Liège, Belgique 2011.
9. Dehandschutter B, Vandycke S, Sintubin M, Vandenberghe N, Wouters L. Brittle fractures and ductile shear bands in argillaceous sediments: inferences from oligocene boom clay (belgium). *Journal of Structural Geology* 2005; **27**(6):1095–1112.
10. Horseman S, Winter M, Enwistle D. Geotechnical characterization of boom clay in relation to the disposal of radioactive waste. *Technical Report*, Commission of the European Communities 1987.
11. Giraud A, Giot R, Homand F, Koriche A. Permeability identification of a weakly permeable partially saturated porous rock. *Transport in porous media* 2007; **69**(2):259–280.
12. Kowalski SJ. *Thermomechanics of drying processes*, vol. 8. Springer Science & Business Media, 2012.
13. Kemp IC, Fyhr BC, Laurent S, Roques MA, Groenewold CE, Tsotsas E, Sereno AA, Bonazzi CB, Bimbenet JJ, Kind M. Methods for processing experimental drying kinetics data. *Drying Technology* 2001; **19**(1):15–34.
14. Léonard A, Blacher S, Marchot P, Crine M. Use of x-ray microtomography to follow the convective heat drying of wastewater sludges. *Drying Technology* 2002; **20**(4-5):1053–1069.
15. Gerard P, Léonard A, Masekanya JP, Charlier R, Collin F. Study of the soil–atmosphere moisture exchanges through convective drying tests in non-isothermal conditions. *International journal for numerical and analytical methods in geomechanics* 2010; **34**(12):1297–1320.
16. Musielak G, Jacek B. Non-linear heat and mass transfer during convective drying of kaolin cylinder under non-steady conditions. *Transport in porous media* 2007; **66**(1-2):121–134.
17. Idso S, Reginato R, Jackson R, Kimball B, Nakayama F. The three stages of drying of a field soil. *Soil Science Society of America Journal* 1974; **38**(5):831–837.
18. Nadeau JP, Puiggali JR. Séchage: des processus physiques aux procédés industriels 1995; .
19. Geankoplis C. Drying of process materials. *Transport processes and unit operations* 1993; :520–583.
20. ONDRAF/NIRAS. Technical overview of the safir 2 report: Safety assessment and feasibility interim report 2. *Technical Report* 2001.
21. Baldi G, Hueckel T, Peano A, Pellegrini R. Developments in modelling of thermohydro-geomechanical behaviour of boom clay and clay-based buffer materials (volume 2). *Technical Report*, Commission of the European Communities 1991.
22. Chen G, Sillen X, Verstricht J, Li XL. Atlas iii in situ heating test in boom clay: Field data, observation and interpretation. *Computers and Geotechnics* 2011; **38**(5):683–696.
23. Sultan N. Etude du comportement thermo-mécanique de l'argile de boom: expériences et modélisation. *THESE DE DOCTORAT PRESENTEE A L'ECOLE NATIONALE DES PONTS ET CHAUSSEES-SPECIALITE: GEOTECHNIQUE* 1997; .
24. Wemaere I, Marivoet J, Labat S. Hydraulic conductivity variability of the boom clay in north-east belgium based on four core drilled boreholes. *Physics and Chemistry of the Earth, Parts A/B/C* 2008; **33**:S24–S36.
25. Aertsens M, Wemaere I, Wouters L. Spatial variability of transport parameters in the boom clay. *Applied Clay Science* 2004; **26**(1):37–45.
26. Blümling P, Bernier F, Lebon P, Martin CD. The excavation damaged zone in clay formations time-dependent behaviour and influence on performance assessment. *Physics and Chemistry of the Earth, Parts A/B/C* 2007; **32**(8):588–599.
27. Leonard A. Étude du séchage convectif des boues de station dépuration - suivi de la texture par microtomographie à rayon x. PhD Thesis, Université de Liège, Belgique 2002.
28. Vincent L, Soille P. Watersheds in digital spaces: An efficient algorithm based on immersion simulations. *IEEE Transactions on Pattern Analysis and Machine Intelligence* Jun 1991; **13**(6):583–598.
29. Plougonven E, Bernard D. A rigid registration method for the study of microgeometry evolution of limestone during dissolution by acidic water. *Advances in X-ray tomography for geomaterials*, 2006; 349–354.
30. Elzinga J, Hearn DW. Geometrical solutions for some minimax location problems. *Transportation Science* 1972; **6**(4):379–394.
31. Lanczos C. *Applied analysis*. Courier Corporation, 1988.
32. Lehmann P, Assouline S, Or D. Characteristic lengths affecting evaporative drying of porous media. *Physical Review E* 2008; **77**(5):056 309.
33. Yiotis A, Boudouvis A, Stubos A, Tsimpanogiannis I, Yortsos Y. Effect of liquid films on the isothermal drying of porous media. *Physical Review E* 2003; **68**(3):037 303.
34. Gerard P, Charlier R, Chambon R, Collin F. Influence of evaporation and seepage on the convergence of a ventilated cavity. *Water resources research* 2008; **44**(5).

35. Léonard A, Blacher S, Marchot P, Pirard JP, Crine M. Convective drying of wastewater sludges: Influence of air temperature, superficial velocity, and humidity on the kinetics. *Drying technology* 2005; **23**(8):1667–1679.
36. Van Genuchten MT. A closed-form equation for predicting the hydraulic conductivity of unsaturated soils. *Soil science society of America journal* 1980; **44**(5):892–898.
37. Coll C. Endommagement des roches argileuses et perméabilité induite au voisinage d'ouvrages souterrains. PhD Thesis, Université Joseph-Fourier-Grenoble I 2005.
38. Hueckel T, Borsetto M, Peano A. Modelling of coupled thermo-elastoplastic-hydraulic response of clays subjected to nuclear waste heat. *ISMES publ./Inst. sperimentale modelli e strutture (Bergamo, Italia)* 1988; .
39. Laloui L, Cekerevac C, Vulliet L. Thermo-plasticity of clays: a simple constitutive approach. *International Workshop on Environmental Geomechanics. Sous la direction de L. Vulliet, L. Laloui et B. Schrefler. Éditions EPFL Press*, 2002; 45–58.
40. Gens A, Alonso E. A framework for the behaviour of unsaturated expansive clays. *Canadian Geotechnical Journal* 1992; **29**(6):1013–1032.
41. Modaressi H, Laloui L. A thermo-viscoplastic constitutive model for clays. *International journal for numerical and analytical methods in geomechanics* 1997; **21**(5):313–335.
42. Collin F, Li XL, Radu JP, Charlier R. Thermo-hydro-mechanical coupling in clay barriers. *Engineering Geology* 2002; **64**(2):179–193.
43. Wouters L, Vandenberghe N. *Géologie de la Campine: essai de synthèse*. ONDRAF, 1994.
44. Garnier J. Tassement et contraintes: influence de la rigidité de la fondation et de l'anisotropie du massif. PhD Thesis 1973.
45. Gatmiri B. Réponse d'un massif sous-marin à l'action de la houle. PhD Thesis, Ecole Nationale des Ponts et Chaussées 1989.
46. Gerard P. Impact des transferts de gaz sur le comportement poro-mécanique des matériaux argileux. PhD Thesis, Thèse de doctorat. Université de Liège, Belgium 2011.
47. Cerfontaine B, Dieudonné AC, Radu JP, Collin F, Charlier R. 3d zero-thickness coupled interface finite element: formulation and application. *Computers and Geotechnics* 2015; **69**:124–140.

DOI: 10.1002/nag